Recent Advances in Quantum Spin Liquids in Two-Dimensional Kagome System $YCu_3(OH)_{6+x}X_{3-x}$ (X = Cl, Br)

Shiliang Li[1,2*]

[1]*Beijing National Laboratory for Condensed Matter Physics, Institute of Physics, Chinese Academy of Sciences, Beijing 100190, China*
[2]*School of Physical Sciences, University of Chinese Academy of Sciences, Beijing 100190, China*

(Received 2 April 2025; accepted manuscript online 25 June 2025)

The two-dimensional kagome lattice serves as a prototypical platform for exploring quantum spin liquids owing to its pronounced geometric frustration. Substantial advancements have been achieved in herbertsmithite and its structural analogs. These quantum spin liquid candidates exhibit large superexchange interactions yet resist magnetic ordering down to the lowest measurable temperatures, which are typically three or four orders of magnitude below the energy scale of the primary exchange energies. Nevertheless, the existence of unavoidable intrinsic interlayer magnetic impurities leads to persistent debates on their ground states. A breakthrough emerged with the discovery of $YCu_3(OH)_{6+x}X_{3-x}$ (X = Cl, Br), a novel material family rigorously verified to eliminate magnetic impurity interference. This short review highlights critical advances in these materials, emphasizing experimental signatures consistent with a Dirac quantum spin liquid and the observation of a one-ninth magnetization plateau and possible quantum oscillations. Local structural characteristics play a crucial role in clarifying the complex emergent quantum phenomena of these materials. Collectively, these findings establish this material class as a promising platform for investigating quantum spin liquid behavior in two-dimensional kagome lattices.

DOI: 10.1088/0256-307X/42/7/070716 CSTR: 32039.14.0256-307X.42.7.070716

1. Introduction. The concept of quantum spin liquids (QSLs) was first proposed over 50 years ago as a ground state alternative to the Néel antiferromagnetic (AFM) order for $S = 1/2$ systems.[1] Understanding QSLs necessitates moving beyond the Landau–Ginzburg–Wilson paradigm of symmetry breaking, as these states are not defined by conventional order parameters but are instead characterized by long-range entanglement and fractionalized, nonlocal excitations.[2–5] While QSLs have been rigorously established in solvable models, such as Kitaev's honeycomb model and the toric code,[6,7] their theoretical investigation in generic frustrated systems remains challenging. Experimental confirmation of QSLs faces even greater challenges due to the lack of probes capable of directly detecting fractionalized excitations, leaving all studied QSL materials as provisional candidates rather than confirmed QSLs.

The two-dimensional (2D) kagome lattice, composed of corner-sharing triangles, hosts the most pronounced geometric magnetic frustration in 2D AFM systems. Rigorous theories have been proposed, spanning both gapped and gapless QSL phases in the 2D kagome Heisenberg antiferromagnet (KHA).[8–25] In these QSLs, the spinon, an $S = 1/2$ charge-neutral fractionalized quasiparticle, emerges due to the long-range entanglements of spins. Two paradigmatic ground states are Z_2 QSL and U(1) Dirac QSL. In the former, all excitations, including spinons, are gapped, and the low-energy physics is governed by Z_2 topological order characterized by a Z_2 gauge field. The U(1) Dirac QSL can be realized through fermionic spinons with a Dirac spectrum coupled to an emergent U(1) gauge field. These promising theoretical results have stimulated great experimental efforts to identify QSLs in kagome materials.

Among various kagome materials investigated for QSLs, herbertsmithite stands out as one of the most promising candidates.[26,27] Named in honor of British mineralogist G. F. Herbert Smith, who discovered the mineral paratacamite $[Cu_4(OH)_6Cl_2]$,[28] herbertsmithite is synthesized by substituting interlayer Cu^{2+} ions in paratacamite with Zn^{2+}, leaving the remaining Cu^{2+} ions ($S = 1/2$) to form perfect kagome planes.[29] Notably, $ZnCu_3(OH)_6Cl_2$ exists as a polymorph with herbertsmithite and kapellasite, the distinction being that Zn^{2+} ions occupy positions between and within the kagome layers, respectively.[30] The magnetic interactions in herbertsmithite are well described by the KHA model, incorporating a c-axis Dzyaloshinsky–Moriya (DM) interaction.[31] With a dominant nearest-neighbor superexchange interaction ($J \sim 200$ K), herbertsmithite exhibits no magnetic ordering down to 20 mK.[32] This large J is critical, as it ensures that both the experimental temperature and energy scales could reach orders of magnitude below J, thereby revealing the intrinsic ground-state properties. Inelastic neutron scattering (INS) studies on single-crystal herbertsmithite have uncovered a spin continuum characterized by weak momentum and energy dependence,[33] which aligns with the theoretical predictions of two-spinon excitations

*Corresponding author. Email: slli@iphy.ac.cn
© 2025 Chinese Physical Society and IOP Publishing Ltd. All rights, including for text and data mining, AI training, and similar technologies, are reserved.

detectable via neutrons,[34,35] solidifying herbertsmithite as a leading QSL candidate.

However, the ground-state nature of herbertsmithite remains actively debated. Initial studies proposed a gapless ground state, supported by the nearly T^2 dependence of the specific heat[36] and spin excitations persisting down to 0.1 meV in INS.[33,36,37] Further evidence emerged from quantum scaling behaviors in the low-energy imaginary part of magnetic susceptibility (χ'') and nuclear magnetic resonance (NMR) spectra,[38–40] indicating power-law spin correlations. These results are consistent with the expectation for a U(1) Dirac QSL.[13] However, subsequent studies revealed that both low-temperature specific heat and low-energy spin excitations are predominantly governed by weakly correlated magnetic impurities.[41,42] This impurity dominance stems from approximately 15% Cu^{2+} ions occupying Zn^{2+} sites, acting as magnetic impurities.[43] Advanced NMR and INS analyses attempting to isolate kagome-layer spin excitations suggest a gapped magnetic system,[44,45] though methodological reliability remains contentious, given a conflicting NMR report of a gapless ground state.[46] Critically, impurity subtraction approaches may be inadequate, as interlayer spins can couple coherently to kagome spins, inducing emergent gapless behavior in otherwise gapped systems.[47] The issues of intrinsic magnetic impurities persist in many herbertsmithite analogs, such as $MgCu_3(OH)_6Cl_2$, $ZnCu_3(OH)_6SO_4$, $Cu_3Zn(OH)_6FBr$, and $Cu_3Zn(OH)_6FCl$.[48–53] Given current limitations in probing nonlocal low-energy excitations,[47] synthesizing impurity-free kagome systems has become a pivotal frontier in QSL research.

In recent years, new kagome compounds $YCu_3(OH)_{6+x}X_{3-x}$ (X = Cl, Br) have been successfully synthesized, circumventing the intrinsic magnetic impurity problem plaguing herbertsmithite due to their unique structures. In principle, this impurity-free architecture positions it as a superior platform for probing pristine QSLs. Indeed, experimental evidence has been found for the existence of a Dirac QSL and one-ninth magnetization plateau at high fields, both of which have been highly anticipated theoretically in a KHA but had not been observed experimentally. However, the system has its own challenges due to structural disorders. This review will provide a brief introduction to their structural and magnetic properties.

2. Structures of $YCu_3(OH)_{6+x}X_{3-x}$. Both the Cl- and Br-based compounds were first reported by J.-X. Mi's group.[54,56] Figure 1(a) shows the crystal structure of $YCu_3(OH)_6Cl_3$ (YCu_3-Cl).[54] The structure can be viewed as derived from kapellasite with Zn^{2+} replaced by Y3+ and an additional Cl^- to maintain charge balance. The compound crystallizes in the trigonal structure with the space group $P\bar{3}m1$. Each Cu^{2+} cation is surrounded by four equatorial O^- and two apical Cl^- anions, forming a $[CuO_4Cl_2]$ octahedron. The Y^{3+} cations occupy the centers of the hexagons within the kagome planes and are bridged by Cl^- anions along the c axis. A partial vertical displacement ($< 10\%$) of Y^{3+} ions from the central position may occur. Structural refinement confirms no detectable mixing between Y^{3+} and Cu^{2+} ions, consistent with their distinct valence states and ion radii.

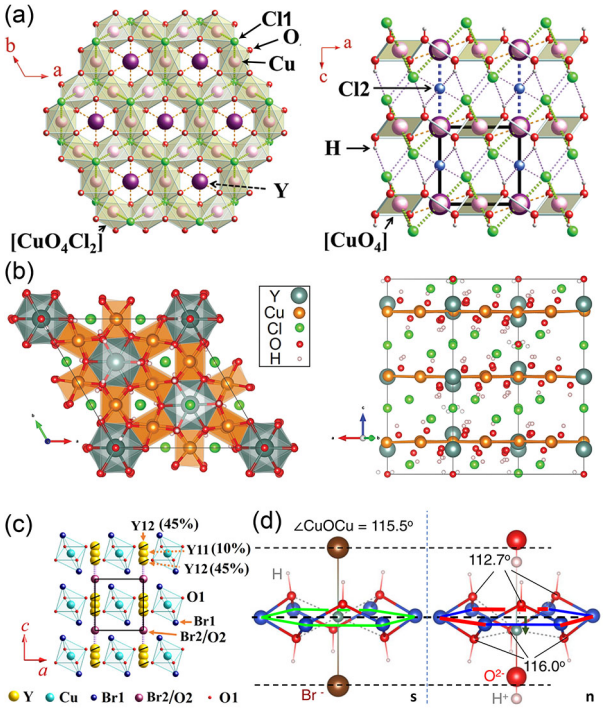

Fig. 1. Crystal structures of $YCu_3(OH)_{6+x}X_{3-x}$ (X = Cl, Br). (a) Crystal structure of YCu_3-Cl with (left) location of Y atoms within the layer consisting of $[CuO_4Cl_2]$ octahedra and (right) side view along the b axis.[54] Dark lines represent the unit cell. (b) Crystal structure of Y_3Cu_9-Cl with (left) top view of the kagome layer and (right) side view.[55] The solid lines represent the unit cell. (c) Crystal structure of YCu_3-Br.[56] The solid lines represent the unit cell. (d) Local structures of YCu_3-Br for supercells containing symmetric (left) and nonsymmetric (right) environments,[57] calculated by DFT. The angles are for Cu-O-Cu.

While the above compound has been grown by low-temperature solid-state reaction, it can also be synthesized via the hydrothermal method.[55] However, in this case, 1/3 of the Cl^- anions at Cl2 site [Fig. 1(a)] are replaced by $(OH)^-$, altering the structure to $R\bar{3}$, as shown in Fig. 1(b). The molecular formula is thus expressed as $YCu_3(OH)_6O_xCl_{3-x}$ ($x = 1/3$),[58] $Y_3Cu_9(OH)_{18}[Cl_8(OH)]$,[59] or $Y_3Cu_9(OH)_{19}Cl_8$[60] (Y_3Cu_9-Cl). The a and c lattice parameters increase approximately $\sqrt{3}$ and 3 times of those in YCu_3-Cl, respectively. The structure features two nonequivalent Y sites with full occupancy, causing slight deviations of Cu^{2+} ions from the ideal kagome geometry and resulting in three distinct nearest-neighbor Cu-Cu bond lengths and Cu-O-Cu bond angles. Notably, the same structure has also been identified in $Y_3Cu_9(OH)_{19}Br_8$ (Y_3Cu_9-Br) and $LuCu_3(OH)_6Br_2[Br_x(OH)_{1-x}]$ ($LuCu_3$-Br).[61,62]

A third type of structure is found in $YCu_3(OH)_6Br_2[Br_{1-x}(OH)_x]$ (YCu_3-Br), as shown in Fig. 1(c).[56] The space group is $P\bar{3}m1$, and the Cu^{2+} kagome planes are geometrically ideal. Compared to YCu_3-Cl, there are two structural distinctions. First, the Br2 site in YCu_3-Br exhibits mixed occupancy by Br^- and $(OH)^-$ ions. Second, two nonequivalent Y^{3+} sites exist—one within the kagome plane (Y11) and another displaced from the plane (Y22). This displacement

arises because the polar $(OH)^-$ ligand pulls the coordinated Y_{3+} ion out of the kagome plane, inducing alternating Cu-O-Cu bond angles within the Cu^{2+} hexagon, as shown in Fig. 1(d).[57] Thus, the local coordination geometry around these hexagons resembles that in Y_3Cu_9-Cl.[55] Notably, these results are derived from density functional theory (DFT) calculations, and experimental validation is required to fully resolve the local structure of YCu_3-Br. Intriguingly, a series of mixed-halide samples $YCu_3(OH)_6[(Cl_xBr_{1-x})_{3-y}(OH)_y]$ (YCu_3-ClBr) have been synthesized, retaining the $P\bar{3}m1$ structure for $x \leq 0.9$.[63] However, single-crystal X-ray diffraction of YCu_3-Br can be indexed to the $R\bar{3}$ space group, through structural refinements show low reliability.[56] It remains unclear whether this stems from coexisting structural phases within the crystal or a more complex superstructure.[61]

3. Magnetic Properties of YCu_3-Cl. We start by introducing the magnetic properties of YCu_3-Cl. While the original goal of synthesizing kagome materials free of magnetic impurities is achieved, YCu_3-Cl unfortunately exhibits AFM ordering below approximately 15 K.[54,64–66] Figure 2(a) shows the temperature dependence of DC magnetic susceptibility of YCu_3Cl under different magnetic fields.[64] Fitting high-temperature data with the Curie–Weiss law yields a Weiss temperature of about 100 K, indicating large AFM interactions. A steep increase is observed below about 15 K in weak magnetic fields, consistent with the onset of long-range AFM order as evidenced by muon-spin relaxation (μSR) measurements.[64] Below approximately 12 K, a small hump or plateau appears. Notably, a splitting between zero-field-cooled and field-cooled processes appears below 6.5 K. This splitting is suppressed above 100 mT, while the hump vanishes completely at 5 T.

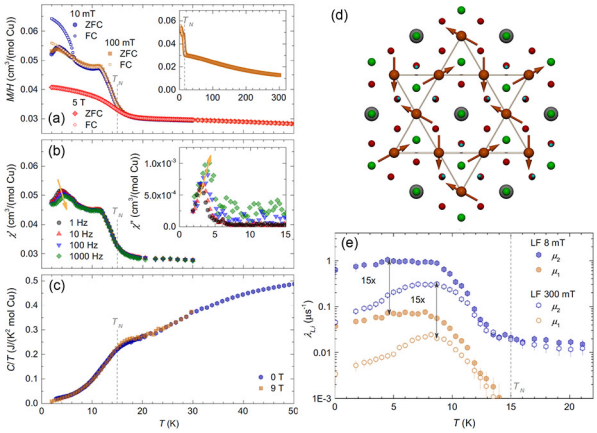

Fig. 2. Magnetic ordering and persistent spin dynamics in YCu_3-Cl. (a) DC magnetization normalized by the applied magnetic field.[64] The inset shows the data with a range up to 300 K. (b) The real part χ' and the imaginary part χ'' (inset) of the AC susceptibility measured in an AC field of 0.6 mT and zero DC magnetic field.[64] (c) The temperature dependence of the specific heat C/T at 0 and 9 T.[64] (d) The coplanar magnetic structure (arrows) with negative vector spin chirality corresponding to the magnetic propagation vector $\boldsymbol{k} = (0, 0, 0.5)$.[65] (e) The temperature dependence of the longitudinal muon-spin relaxation rate for the two μSR components μ_i.[64] The vertical dashed lines in (a), (b), (c), and (e) indicate the magnetic ordering temperature T_N.

AC magnetic susceptibility measurements suggests a possible glassy transition. As shown in Fig. 2(b), the real component of the AC susceptibility χ' shows a frequency-dependent peak between about 3 to 4 K, shifting to higher temperatures with increasing frequency. The imaginary component χ'' exhibits similar frequency-dependent behavior. These features may originate from a tiny fraction (∼0.1%) of clinoatacamite $Cu_4(OH)_6Cl_2$, which undergoes a spin-glass transition at 6.4 K.[67] Specific heat over temperature (C/T) data in Fig. 2(c) display a broad, nearly field-independent hump at about 15 K. Although initially attributed to AFM ordering,[64] recent studies propose that DM interactions or structural distortions may provide plausible explanations.[61,66]

Neutron diffraction measurements have revealed magnetic peaks with the propagation vector $\boldsymbol{k} = (0, 0, 0.5)$.[65] The magnetic structure of the AFM order in YCu_3-Cl is determined to be a coplanar 120° state with negative vector spin chirality, exhibiting an ordered moment of $0.42(2)\mu_B$, as shown in Fig. 2(d). This aligns with theoretical predictions that the out-of-plane DM component D_z can stabilize negative vector chirality in the kagome lattice when $D_z > 0$.[68] The DM anisotropy, ubiquitous in herbertsmithite and its analogs, originates from spin-orbit-coupling-induced relativistic corrections to the isotropic Heisenberg Hamiltonian. Its magnitude is on the order of $D/J_1 \approx \Delta g/g$, where J_1 is the nearest superexchange, g is the g-factor, and Δg is its anisotropy.[31,69] In YCu_3-Cl, electron spin resonance confirms $D_z/J_1 \approx 0.25$ with negligible in-plane DM components.[66] Notably, the temperature dependence of the magnetic susceptibility above about 20 K and the broad specific heat hump near 15 K are both consistent with a framework based on the Heisenberg model plus the DM interactions. Intriguingly, μSR measurements show that the muon relaxation rate in the longitudinal fields increases below the AFM transition temperature T_N, peaking broadly at temperatures far below T_N [Fig. 2(e)].[64] At zero-temperature limits, the relaxation rates suggest persistent spin fluctuations in the ordered state, potentially originating from either spin-loop structures or a coexistence of partial order and disorder.[64]

As introduced above, the structure of YCu_3-Cl changes from $P\bar{3}m1$ to $R\bar{3}$ due to partial substitution of Cl^- by $(OH)^-$ when synthesized via the hydrothermal method. The low-temperature magnetic properties of Y_3Cu_9-Cl exhibit marked inconsistencies across different studies. As shown in Fig. 3(a), the specific heat divided by temperature (C/T) displays a broad hump near 15 K and a relatively sharper hump around 2 K (blue and black squares, respectively) in Refs. [58,59]. In another study, the high-temperature hump shifts to higher temperatures, while the low-temperature hump becomes strongly enhanced [open red circles in Fig. 3(a)].[58] Notably, additional sharp peaks emerge above 30 K in a separate report, and the low-temperature hump evolves into a sharp peak, signaling a magnetic transition [solid circles in Fig. 3(a)].[60] These discrepancies have been attributed to sample quality variations, although no quantitative standards for assessing sample quality have been established.

Here we focus on the results of the latter sample,

which has been extensively characterized through multiple experimental techniques.[60] Thermal expansion measurements along the c axis reveal three peaks, as shown in Fig. 3(b). Two peaks around 32 K correlate with the high-temperature peaks observed in C/T. An additional small anomaly is found around 13 K but is absent in specific heat data. Notably, no corresponding signature is observed in magnetic susceptibility measurements. Neutron diffraction studies confirm no emergent new crystal Bragg peaks at low temperatures, ruling out significant temperature-dependent structural modifications. Rather a rapid intensity variation in Bragg peaks is detected around 32 K, likely attributable to freezing of mobile deuterium or hydrogen atoms at low temperatures. These structural distortions are further confirmed by ^{35}Cl NMR, where line broadening at triangular sites and splitting at hexagonal sites indicate symmetry reduction. The 13-K thermal expansion anomaly is attributed to a secondary structural transition. Intriguingly, similar structural distortion mechanism is also proposed in Y_3Cu_9-Br.[61]

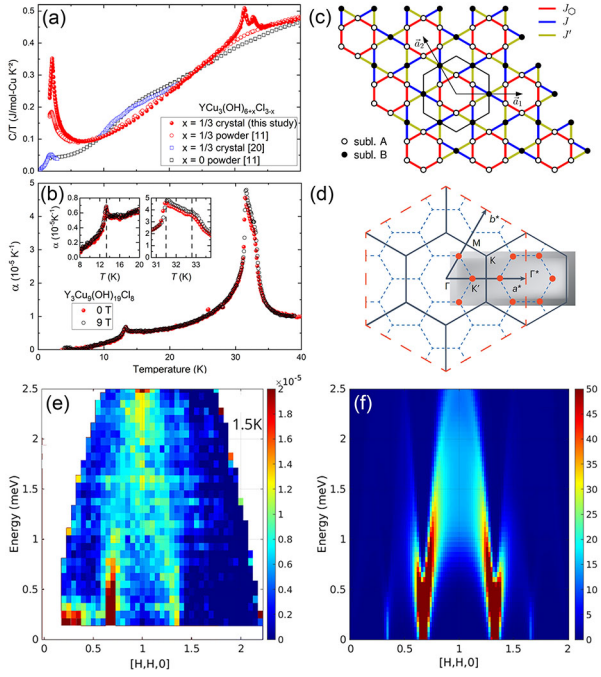

Fig. 3. Magnetic properties and spin excitations in Y_3Cu_9-Cl. (a) Temperature dependence of the specific heat C/T for various Y_3Cu_9-Cl ($x = 1/3$) and YCu_3-Cl ($x = 0$) samples.[58–60] The reference numbers are from the original figure in Ref. [60]. (b) Temperature dependence of the thermal expansion coefficient α along the c direction.[60] The insets show enlarged views of the peaks in α. (c) Schematic illustration of the three exchange couplings shown in red, blue, and green.[70] a_1 and a_2 are the Bravais vectors of the enlarged unit cell in this model. (d) Sketch of the in-plane reciprocal space. The black solid line and the red and blue dashed lines represent the Brillouin zone of the kagome lattice, the extended kagome lattice, and the enlarged unit cell in (c), respectively.[71] (e) Spin excitations as a function of E, and $\boldsymbol{Q}$ along the $[H, 0]$ direction at 1.5 K with the 5 K INS data subtracted as background.[60] (f) Spin-wave simulations based on the $3J$ model.[60] Both (e) and (f) use the Brillouin zone in the enlarged unit cell corresponding to the $R\bar{3}$ space group.

Multiple experimental techniques, including NMR, μSR, and neutron diffraction, reveal a long-range magnetic ordering at 2.1 K.[60] The magnetic peak positions match the theoretically proposed so-called $(1/3, 1/3)$ coplanar AFM order. In this model, the three nearest-neighbor superexchange couplings within the kagome lattice triangles exhibit ordered differentiation, as shown in Fig. 3(c),[70] directly corresponding to the variations of Cu-O-Cu bond angles [Fig. 1(b)]. This "$3J$" model leads to a configuration where one third of hexagons retain uniform exchange bonds, while the remaining two-thirds adopt alternate bonds. This symmetry-breaking arrangement triples the in-plane unit cell size. Classical Monte Carlo simulations predict two noncollinear coplanar magnetic phases with ordering wave vector $\boldsymbol{Q} = (1/3, 1/3)$ in the expanded unit cell [red solid circles in Fig. 3(d)]. INS measurements further resolve damped magnons, well described by linear spin-wave theory incorporating the $3J$ model with controlled exchange disorder.[60]

4. Magnetic Properties of YCu_3-Br. While both magnetically ordered and disordered phases have been observed in the YCu_3-Cl system, replacing Cl with Br always results in the magnetically disordered phase, with a single exception reported in Y_3Cu_9-Br,[61] which has the $R\bar{3}$ structure. Comprehensive characterization via specific heat, magnetic susceptibility, NMR, and μSR has demonstrated the absence of magnetic ordering in the YCu_3-Br system down to 50 mK,[72–75] which is less than 0.1% of the Weiss temperature.[72,76] The low-temperature specific heat shows a T^2 dependence below about 0.7 K,[72] which is more clearly observed by plotting C/T vs T to reveal $C/T = \alpha T$, as shown in Fig. 4(a). Under magnetic fields,

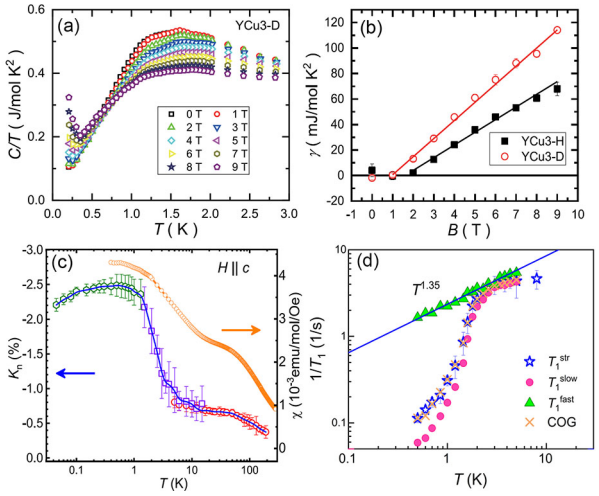

Fig. 4. Specific heat and NMR results of YCu_3-Br. (a) Temperature dependence of C/T at different fields for deuterated YCu_3-Br sample.[72] (b) Field dependence of the linear-T term in deuterated (YCu3-D) and undeuterated (YCu3-H) samples.[72] The solid lines are fitted results using the linear function. (c) Temperature dependence of Knight shift K_n of ^{81}Br (circles and squares) and ^{79}(hexagons) at fields given in Ref. [73]. Magnetic susceptibility data are adapted from Ref. [72]. (d) Temperature dependence of $1/T_1^{\text{slow}}$ (circles), $1/T_1^{\text{fast}}$ (triangles), $1/T_1^{\text{str}}$ (stars), and the center of gravity (crosses) from the ^{63,65}Cu NQR measurements.[74]

the low-temperature specific heat follows $C/T = \gamma + \alpha T$, suggesting the appearance of a linear-T term. Figure 4(a) shows C/T as a function of T in a deuterated YCu_3-Br sample, where the large contribution to the specific heat from nuclear Schottky anomalies of hydrogen ions is significantly suppressed.[72] Figure 4(b) plots the field dependence of γ for both deuterated and undeuterated samples,[72] which exhibit linear behavior above certain fields. The variation between different samples arises from structural differences discussed later. These behaviors align with theoretical predictions of a U(1) Dirac QSL on a kagome lattice.[13] At zero field and with four two-component Dirac fermions, the theory provides

$$C = \frac{72\zeta(3)\pi k_{\mathrm{B}}^3 A}{(2\pi\hbar\nu_{\mathrm{F}})^2} T^2 = \alpha T^2, \tag{1}$$

where A is the area of the 2D system and ν_{F} is the Dirac spinon velocity. At high magnetic fields, the spinons form Fermi pockets, yielding a linear term,

$$C = \frac{8\pi^3 k_{\mathrm{B}}^2 A \mu_{\mathrm{B}} B}{3(2\pi\hbar\nu_{\mathrm{F}})2} T = \gamma T. \tag{2}$$

Despite qualitative agreement, the ratio $(\mathrm{d}\gamma/\mathrm{F}B)/\alpha$ is only about 1/7 of the theoretical value (≈0.21 K/T), which is yet to be resolved.

NMR measurements on Br nuclei reveal the temperature dependence of the Knight shift that mirrors bulk magnetic susceptibility at high temperatures, as shown in Fig. 4(c).[73] The Knight shift increases sharply with decreasing temperature below about 4 K and becomes almost temperature independent below about 1 K. Similar low-temperature saturation is observed in magnetic susceptibility derived from torque measurements.[75] In a Heisenberg system, the uniform DC magnetic susceptibility is associated with the spin-dependent density of states; thus, the temperature invariance of both Knight shift and susceptibility appears inconsistent with the Dirac QSL scenario, where gapless spinons should induce T^2 dependence of the density of states as observed in specific heat. This paradox has promoted proposals involving strong localization of spinons or even bosonic quasiparticles.[73,75] Critically, however, the inevitable DM interactions in these materials[66,77] imply that bulk susceptibility cannot be a good representative of the density states of low-energy spinons.[3] Notably, the spin-lattice relaxation rate $1/T_1$ displays strong anisotropy between $H \parallel ab$ and $H \parallel c$ at low temperatures, whereas $1/T_2$ remains isotropic, suggesting distinct relaxation mechanisms.[73] Furthermore, $1/T_2$ exhibits a linear T-dependence below 0.4 K, potentially signaling gapless excitations with a Fermi surface under fields.

μSR measurements reveal no coherent oscillations down to 50 mK and a one-third recovery of the muon polarization at long times, which further solidifies the absence of static magnetic ordering.[24] The μSR spectra can be modeled by a combination of an exponential component and a Gaussian-relaxing component, suggesting an inhomogeneous mixture of spins with distinct behaviors. This is consistent with zero-field ^{63,65}Cu nuclear quadrupole resonance (NQR) measurements, which reveal two nuclear spin-lattice relaxation rate $1/T_1$, where the slow component T_1^{slow} is nearly two orders of magnitude smaller than the fast component T_1^{fast}.[74] Intriguingly, $1/T_1^{\mathrm{fast}}$ exhibits a $T^{1.35}$ power-law dependence, while $1/T_1^{\mathrm{slow}}$ is significantly suppressed below 8 K, as shown in Fig. 4(d). These results suggest gapless and gapped excitations, respectively. Notably, the temperature dependence of the gapped excitations cannot be explained by activation due to a well-defined gap, implying the presence of varying spin gaps. Collectively, these findings support the existence of gapless Dirac fermions intermingled with a minor fraction of spin singlets exhibiting energy gaps of varying magnitudes.[74]

INS measurements provide the strongest spectral evidence for Dirac spinons in QSLs. The low-energy spin excitations in YCu_3-Br exhibit exceptional sharpness, localized at six symmetric positions within the second Brillouin zone, as shown in Fig. 5(a).[71] These excitations become broader progressively with increasing energy and interconnect with each other above 1 meV [Fig. 5(b)]. Momentum-resolved analysis along the $[H, 0]$ direction reveals a conical continuum of low-energy spin excitations, as shown through the E–$\boldsymbol{Q}$ intensity mapping in Fig. 5(c). Notably, these excitations also exist in the first Brillouin zone but are much weaker since the integrated intensity follows the structure factor of randomly arranged nearest-neighbor singlets. The observed conical spin continuum aligns

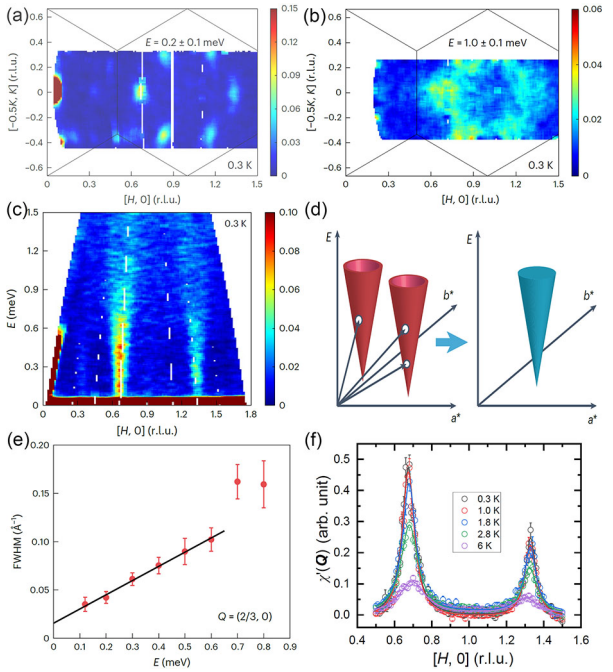

Fig. 5. Spin excitations in YCu_3-Br. (a) and (b) Intensity contour plots of the INS results in the $[H, K]$ zone at 0.2 and 1 meV, respectively.[71] The ± symbol gives the integrated energy range. The solid lines forming the hexagons mark the kagome Brillouin zone. (c) Intensity contour plot as a function of E, and $\boldsymbol{Q}$ along the $[H, 0]$ direction at 0.3 K.[71] (d) Schematic illustration of two Dirac spinons (left) that emerge into a conical spin continuum (right) observable in INS experiments.[71] (e) Energy dependence of the full-width-at-half-maximum (FWHM) around $\boldsymbol{Q} = (2/3, 0)$.[71] (f) $\chi'(\boldsymbol{Q})$ along the $[H, 0]$ direction at several temperatures.[77] The solid lines are fitted results by the Lorentzian function.

rigorously with theoretical predictions for Dirac QSLs,[78–80] where linearly dispersive Dirac spinons generate such a characteristic continuum for two-spinon excitations observable in INS experiments, as shown in Fig. 5(d). The width of the low-energy spin excitations, when fitted with a Lorentzian function, shows a clear linear temperature dependence [Fig. 5(e)]. Its slope provides an estimate of the spinon velocity ($\sim$1 km/s),[71] which can quantitatively derive the coefficient of the quadratic temperature dependence in the specific heat via Eq. (1),[13] robustly supporting the existence of Dirac spinons.

Intriguingly, the $\boldsymbol{Q}$-positions of the low-energy spin excitations in YCu_3-Br coincide precisely with those in Y_3Cu_9-Cl [Fig. 3(e), note that different $\boldsymbol{Q}$ values come from different Brillouin zones defined in Fig. 3(d)], suggesting a fundamental connection with the $3J$ model [Fig. 3(c)] despite their lattice structures being very different. Compared to the damped magnons in Y_3Cu_9-Cl,[60] there are two critical distinctions. First, the low-energy spin excitations in YCu_3-Br are much sharper even through the spin system is not ordered. By using the Kramers–Kronig (KK) relation to obtain the real part of the dynamical susceptibility $\chi'(\boldsymbol{Q})$, the magnetic correlation length is determined to be about 70–80 Å at 0.3 K via Lorentzian fitting $\chi'(\boldsymbol{Q})$ around (2/3, 0)[71,77] [Fig. 5(f)], indicative of long-range power-law correlations of the spin system. Second, the continuum at higher energies retains symmetrical intensity peaking at the center, whereas in Y_3Cu_9-Cl, analogous excitations become asymmetric due to the magnon structural factor and exhibit weaker central intensities [Figs. 3(e) and 3(f)]. Notably, the ability to map whole spectra in YCu_3-Br and derive $\chi'(\boldsymbol{Q})$ via the KK relation allows for cross-validation between INS and other techniques, such as NMR and Raman scattering, provides a new promising methodology in QSL studies.[77]

Besides the intriguing zero-field magnetic properties, the YCu_3-Br system exhibits remarkable phenomena at high fields. Theoretical studies on the $S = 1/2$ KHA model predict fractional magnetization plateaus $M/M_s = 1/9$, 1/3, 5/9, and 7/9, where M_s denotes the saturated magnetic moment.[81,83–85] While the 1/3, 5/9, and 7/9 plateaus can be interpreted through magnon condensation, the 1/9 plateau necessitates an exotic origin, potentially revealing novel physics. However, experimental observation of the 1/9 plateau remained elusive until its recent discovery in YCu_3-Br.[75,76,82,86,87] Figure 6(a) demonstrates the field dependence of magnetization, where the 1/9 plateau appears at about 20 T. The nature of this magnetization is in debate both experimentally and theoretically. The experimental controversy is whether the state at the 1/9 plateau is gapped or gapless. It was reported that $\mathrm{d}M/\mathrm{d}H$ exhibits strong temperature dependence at the field of 1/9 plateau, suggesting a gapless state.[82] However, another group observed temperature-independent magnetization, demonstrating that it is gapped.[86] Figure 6(b) shows the temperature dependence of the specific heat C/T at the 1/9 plateau,[87] which is at slightly different fields due to different g factors. The C/T data fit well to $\gamma + \beta T$, where γ term exhibits large anisotropy between $H \parallel c$ and $H \parallel ab$, contrasting with the isotropic β. This confirms the gapless nature of the 1/9 plateau, consistent with a Dirac spectrum coexisting with a finite density of states contributed by other Fermi surfaces. Resolving these contradictions demands systematic investigations across measurement techniques and sample batches.

An even more surprising phenomenon is the discovery of quantum oscillations through high-field magnetic torque measurements on YCu_3-Br.[82] While magnetic oscillations due to Landau Level quantization are characteristic for metallic systems, theoretical proposals suggest that charge-neutral spinons in certain QSL could exhibit analogous behavior.[88] Magnetic torque measurements reveal a series of dips and peaks above 20 T, as shown in Fig. 6(d).[82] Second-derivative analysis of magnetic torque τ with respect to H clearly demonstrates the presence of oscillations, as shown in Fig. 6(e). Crucially, the angular dependence of these oscillations rules out the possibility of multiple magnetic transitions and suggests the orbital origin of the oscillations. Moreover, the temperature dependence of the amplitude after fast fourier transformation (FFT) can be well fitted by the Lifshitz–Kosevich (LK) formula, which describes the oscillation behavior of fermions, leading to an effective mass m^* of about four times that of a bare electron, m_e, as shown in Fig. 6(f). These results can be understood as a QSL with Dirac spinons coupled to an emergent gauge field.[82] Note that the theoretical model in Ref. [82] is not directly associated with the Dirac ground state discussed above, as it gives a state with spinon Fermi surfaces at zero field.

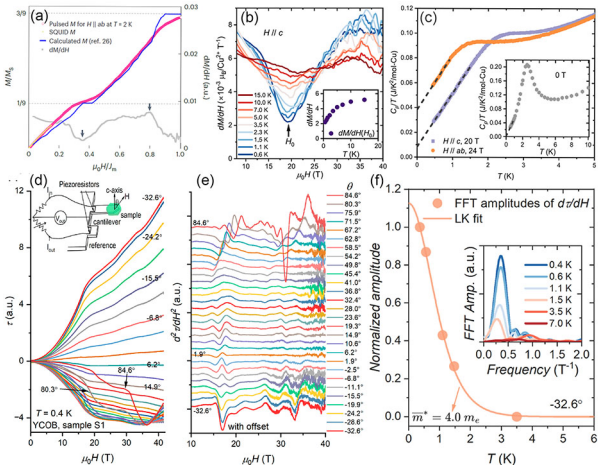

Fig. 6. The 1/9 magnetization plateau and quantum oscillations in YCu_3-Br. (a) Field dependence of the magnetization and its field derivative. M_s denotes the saturation magnetization. The blue line represents the calculated magnetization from Ref. [81]. J_m (=45 K) is the exchange interaction. (b) Field dependence of $\mathrm{d}M/\mathrm{d}H$ at various temperatures. The inset shows the temperature dependence of $\mathrm{d}M/\mathrm{d}H$ at H_0.[82] (c) Temperature dependence of C/T at 20 and 24 T for the field parallel to c axis and ab plane, respectively.[82] The dashed lines are the linear fitting results. The inset shows C/T at zero field. (d) and (e) Field dependence of τ and $\mathrm{d}^2\tau/\mathrm{d}H^2$, respectively, at different angles between the field and c axis.[82] The inset in (d) illustrates the piezoresistive cantilever design for torque measurements. (f) Temperature dependence of the normalized FFT amplitude of the $\mathrm{d}\tau/\mathrm{d}H$ oscillatory patterns after background subtraction.[82] The solid curve represents LK fit results. The inset shows the FFT analysis within the 24–35.7 T window.

Table 1. A list of the chemical formulas, space groups and ground states for the $YCu_3(OH)_{6+x}X_{3-x}$ system.

Abbreviation	Chemical formula	Space group	Ground states
YCu$_3$-Cl	$YCu_3(OH)_6Cl_3$	$P\bar{3}m1$	AFM ($T_N \approx 15$ K) [54,64–66]
Y$_3$-Cu$_9$-Cl	$Y_3Cu_9(OH)_{18}OCl_8$	$R\bar{3}$	QSL [58]
	$Y_3Cu_9(OH)_{18}[Cl_8(OH)]$	$R\bar{3}$	AFM ($T_N = 11$ K) [59]
	$Y_3Cu_9(OH)_{19}Cl_8$	$R\bar{3}$	AFM ($T_N = 2.1$ K) [60]
YCu$_3$-Br	$YCu_3(OH)_6Br_2[Br_{1-x}(OH)_x]$	$P\bar{3}m1$	QSL [72–75]
Y$_3$Cu$_9$-Br	$Y_3Cu_9(OH)_{19}Br_8$	$R\bar{3}$	Probably AFM [61]
YCu$_3$-ClBr	$YCu_3(OH)_6[(Cl_xBr_{1-x})_{3-y}(OH)_y]$	$P\bar{3}m1$	Adjustable between AFM and QSL [63]

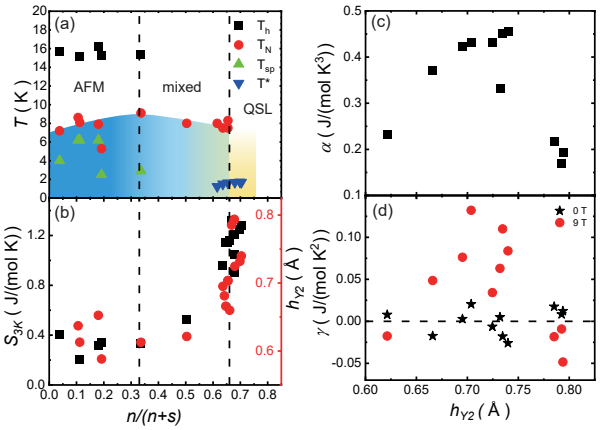

Fig. 7. Magnetic phase diagram and structural dependence of specific heat in YCu$_3$-ClBr. (a) Magnetic phase diagram with the value of $n/(n+s)$ as the variable. [63] (b) The $n/(n+s)$ dependence of the entropy below 3 K and the height of the out-of-plane yttrium h_{Y2}, respectively. [63] (c) and (d) The h_{Y2} dependence of the T^2 coefficient α and the T-linear coefficient γ at 0 and 9 T for the possible QSL and mixed-phases samples with $n/(n+s)$ around 2/3. [63]

From the above discussion, the $YCu_3(OH)_{6+x}X_{3-x}$ system not only demonstrates many intriguing physical properties but also exhibits significant unresolved controversies. Table 1 provides a brief summary of current experimental results for Y-based kagome systems discussed in this review. Notably, discrepancies emerge not only in the reported structural parameters and magnetic properties from different research groups but also in the seemingly contradictory interpretations derived from various experimental techniques. For instance, while the specific-heat and INS data in YCu$_3$-Br provide evidence for Dirac spinons, magnetic susceptibility and Knight shift show no such signatures. Although DM interaction could in principle reconcile this discrepancy, thermal transport measurements give negative results on the formation of spinon Fermi surfaces under magnetic field. [89] The nature of the 1/9 magnetization plateau in YCu$_3$-Br remains particularly contentious, with even identical experimental techniques yielding conflicting conclusions about its gapped or gapless character. A plausible explanation for some of these inconsistencies—particularly prominent in bromine-based samples—lies in the significant structural disorder inherent to this material family. Such disorder likely induces sample-to-sample variations that complicate reproducibility across studies.

In studies of YCu$_3$-ClBr samples (mixed chlorine/bromine systems), magnetic properties are found to depend not on the Cl/Br ratio but on the percentage of alternate-bond hexagons (ABHs). [63] To better comprehend this, we should re-examine the local structure of the hexagons formed by Cu^{2+} ions in Fig. 1(d). These hexagons exist in two distinct configurations: uniform hexagons (UHs) with identical Cu-O-Cu bond angles and ABHs with alternating angles. It should be emphasized that the UHs and ABHs cannot be randomly distributed, as the low-energy spin excitations exhibit sharp peaks, strongly indicative of a local configuration consistent with the one in Y$_3$Cu$_9$-Cl. [60,71] Indeed, single-crystal X-ray diffraction reveals superstructural peaks originating from the $R\bar{3}$ structure. [56] By determining their proportions (s and n), the magnetic ground state of YCu$_3$-ClBr is found to depend on $n/(n+s)$. When $n/(n+s) < 1/3$, the system exhibits a long-range AFM order, whereas a possible QSL state is found for $n/(n+s) \approx 2/3$, as shown in Fig. 7(a). [63] Between them, the system exhibits mixed phases showing properties for both AFM and QSL states, likely due to the phase separation coming from inhomogeneous distributions of UHs and ABHs. Notably, the low-temperature entropy undergoes an abrupt change near $n/(n+s) \approx 2/3$. Analysis of C/T via $\gamma+\alpha T$ fitting directly links specific heat to the vertical displacement of Y^{3+} ions within ABHs relative to the kagome plane, as shown in Figs. 7(c) and 7(d). Interestingly, magnetic susceptibility measurements fail to distinguish samples showing field-induced linear term from those without. These findings establish a profound connection between local crystallography and magnetic properties while underscoring the necessity for extreme caution when interpreting and comparing results across different groups.

5. Conclusions. In conclusion, the kagome $YCu_3(OH)_{6+x}X_{3-x}$ family has emerged as a pivotal platform for probing QSL physics and more. By circumventing the intrinsic impurity limitations of herbertsmithite, these systems offer unprecedented access to pristine kagome-layer magnetism. Key breakthroughs include the observation of a possible Dirac QSL ground state, a 1/9 magnetization plateau, and quantum oscillations. However, persistent controversies—particularly regarding the nature of the ground states and the exotic origin of the 1/9 plateau—highlight the critical role of local structural crystallography and sample-dependent variations. Moving forward, resolving these challenges demands advances in material synthesis, unified theoretical frameworks, and multimodal experimental approaches.

References

[1] Anderson P 1973 *Mater. Res. Bull.* **8** 153
[2] Balents L 2010 *Nature* **464** 199
[3] Savary L and Balents L 2017 *Rep. Prog. Phys.* **80** 016502
[4] Zhou Y, Kanoda K, and Ng T K 2017 *Rev. Mod. Phys.* **89** 025003
[5] Broholm C, Cava R J, Kivelson S A, Nocera D G, Norman M R, and Senthil T 2020 *Science* **367** eaay0668
[6] Kitaev A Y 2003 *Ann. Phys.* **303** 2
[7] Kitaev A Y 2006 *Ann. Phys.* **31** 2
[8] Yan S, Huse D A, and White S R 2011 *Science* **332** 1173
[9] Depenbrock S, McCulloch I P, and Schollwöck U 2012 *Phys. Rev. Lett.* **109** 067201
[10] Jiang H C, Wang Z, and Balents L 2012 *Nat. Phys.* **8** 902
[11] Yang F and Yao H 2012 *Phys. Rev. Lett.* **109** 147209
[12] Mei J W, Chen J Y, He H, and Wen X G 2017 *Phys. Rev. B* **95** 235107
[13] Ran Y, Hermele M, Lee P A, and Wen X G 2007 *Phys. Rev. Lett.* **98** 117205
[14] Hermele M, Ran Y, Lee P A, and Wen X G 2008 *Phys. Rev. B* **77** 224413
[15] Iqbal Y, Becca F, and Poilblanc D 2011 *Phys. Rev. B* **84** 020407
[16] Iqbal Y, Poilblanc D, and Becca F 2014 *Phys. Rev. B* **89** 020407
[17] He Y C, Zaletel M P, Oshikawa M, and Pollmann F 2017 *Phys. Rev. X* **7** 031020
[18] Liao H J, Xie Z Y, Chen J, Liu Z Y, Xie H D, Huang R Z, Normand B, and Xiang T 2017 *Phys. Rev. Lett.* **118** 137202
[19] He Y C, Sheng D N, and Chen Y 2014 *Phys. Rev. Lett.* **112** 137202
[20] Gong S S, Zhu W, Balents L, and Sheng D N 2015 *Phys. Rev. B* **91** 075112
[21] Gong S S, Zhu W, Yang K, Starykh O A, Sheng D N, and Balents L 2016 *Phys. Rev. B* **94** 035154
[22] Wang Y C, Zhang X F, Pollmann F, Cheng M, and Meng Z Y 2018 *Phys. Rev. Lett.* **121** 057202
[23] Sun G Y, Wang Y C, Fang C, Qi Y, Cheng M, and Meng Z Y 2018 *Phys. Rev. Lett.* **121** 077201
[24] Lee C Y, Normand B, and Kao Y J 2018 *Phys. Rev. B* **98** 224414
[25] Prelovšek P, Gomilšek M, Arh T, and Zorko A 2021 *Phys. Rev. B* **103** 014431
[26] Mendels P and Bert F 2016 *Comptes Rendus. Physique* **17** 455
[27] Norman M R 2016 *Rev. Mod. Phys.* **88** 041002
[28] Braithwaite R S W, Mereiter K, Paar W H, and Clark A M 2004 *Mineral Mag.* **68** 527
[29] Shores M P, Nytko E A, Bartlett B M, and Nocera D G 2005 *J. Am. Chem. Soc.* **127** 13462
[30] Colman R H, Ritter C, and Wills A S 2008 *Chem. Mater.* **20** 6897
[31] Zorko A, Nellutla S, van Tol J, Brunel L C, Bert F, Duc F, Trombe J C, de Vries M A, Harrison A, and Mendels P 2008 *Phys. Rev. Lett.* **101** 026405
[32] Mendels P, Bert F, de Vries M A, Olariu A, Harrison A, Duc F, Trombe J C, Lord J S, Amato A, and Baines C 2007 *Phys. Rev. Lett.* **98** 077204
[33] Han T H, Helton J S, Chu S, Nocera D G, Rodriguez-Rivera J A, Broholm C, and Lee Y S 2012 *Nature* **492** 406
[34] Punk M, Chowdhury D, and Sachdev S 2014 *Nat. Phys.* **10** 289
[35] Zhu W, shu Gong S, and Sheng D N 2019 *Proc. Natl. Acad. Sci. U.S.A.* **116** 5437
[36] Helton J S, Matan K, Shores M P, Nytko E A, Bartlett B M, Yoshida Y, Takano Y, Suslov A, Qiu Y, Chung J H, Nocera D G, and Lee Y S 2007 *Phys. Rev. Lett.* **98** 107204
[37] Lee S H, Kikuchi H, Qiu Y, Lake B, Huang Q, Habicht K, and Kiefer K 2007 *Nat. Mater.* **6** 853
[38] Helton J S, Matan K, Shores M P, Nytko E A, Bartlett B M, Qiu Y, Nocera D G, and Lee Y S 2010 *Phys. Rev. Lett.* **104** 147201
[39] Imai T, Nytko E A, Bartlett B M, Shores M P, and Nocera D G 2008 *Phys. Rev. Lett.* **100** 077203
[40] Olariu A, Mendels P, Bert F, Duc F, Trombe J C, de Vries M A, and Harrison A 2008 *Phys. Rev. Lett.* **100** 087202
[41] de Vries M A, Kamenev K V, KockelmannWA, Sanchez-Benitez J, and Harrison A 2008 *Phys. Rev. Lett.* **100** 157205
[42] Nilsen G J, de Vries M A, Stewart J R, Harrison A, and Rønnow H M 2013 *J. Phys.: Condens. Matter* **25** 106001
[43] Freedman D E, Han T H, Prodi A, Müller P, Huang Q Z, Chen Y S, Webb S M, Lee Y S, McQueen T M, and Nocera D G 2010 *J. Am. Chem. Soc.* **132** 16185
[44] Fu M, Imai T, Han T H, and Lee Y S 2015 *Science* **350** 655
[45] Han T H, Norman M R, Wen J J, Rodriguez-Rivera J A, Helton J S, Broholm C, and Lee Y S 2016 *Phys. Rev. B* **94** 060409
[46] Khuntia P, Velazquez M, Barthélemy Q, Bert F, Kermarrec E, Legros A, Bernu B, L Messio A Z, and Mendels P 2020 *Nat. Phys.* **16** 469
[47] Wei Y, Ma X, Feng Z, Zhang Y, Zhang L, Yang H, Qi Y, Meng Z Y, Wang Y C, Shi Y, and Li S 2021 *Chin. Phys. Lett.* **38** 097501
[48] Kermarrec E, Mendels P, Bert F, Colman R H, Wills A S, Strobel P, Bonville P, Hillier A, and Amato A 2011 *Phys. Rev. B* **84** 100401
[49] Li Y, Pan B, Li S, Tong W, Ling L, Yang Z, Wang J, Chen Z, Wu Z, and Zhang Q 2014 *New J. Phys.* **16** 093011
[50] Feng Z, Li Z, Meng X, Yi W, Wei Y, Zhang J, Wang Y C, Jiang W, Liu Z, Li S, Liu F, Luo J, Li S, Zheng G, Meng Z Y, Mei J W, and Shi Y 2017 *Chin. Phys. Lett.* **34** 077502
[51] Wei Y, Feng Z, Lohstroh W, Yu D H, Le D, dela Cruz C, Yi W, Ding Z F, Zhang J, Tan C, Shu L, Wang Y C, Wu H Q, Luo J, Mei J W, Yang F, Sheng X L, Li W, Qi Y, Meng Z Y, Shi Y, and Li S 2017 arXiv:1710.02991 [cond-mat.str-el]
[52] Feng Z, Yi W, Zhu K, Wei Y, Miao S, Ma J, Luo J, Li S, Meng Z Y, and Shi Y 2018 *Chin. Phys. Lett.* **36** 017502
[53] Fu Y, Lin ML, Wang L, Liu Q, Huang L, Jiang W, Hao Z, Liu C, Zhang H, Shi X, Zhang J, Dai J, Yu D, Ye F, Lee P A, Tan P H, and Mei J W 2021 *Nat. Commun.* **12** 3048
[54] Sun W, Huang Y X, Nokhrin S, Pan Y, and Mi J X 2016 *J. Mater. Chem. C* **4** 8772
[55] Puphal P, Bolte M, Sheptyakov D, Pustogow A, Kliemt K, Dressel M, Baenitz M, and Krellner C 2017 *J. Mater. Chem. C* **5** 2629
[56] Chen X H, Huang Y X, Pan Y, and Mi J X 2020 *J. Magn. Magn. Mater.* **512** 167066
[57] Liu J, Yuan L, Li X, Li B, Zhao K, Liao H, and Li Y 2022 *Phys. Rev. B* **105** 024418
[58] Barthélemy Q, Puphal P, Zoch K M, Krellner C, Luetkens H, Baines C, Sheptyakov D, Kermarrec E, Mendels P, and Bert F 2019 *Phys. Rev. Materials* **3** 074401
[59] Sun W, Arh T, Gomilšek M, Koželj P, Vrtnik S, Herak M, Mi J X, and Zorko A 2021 *Phys. Rev. Mater.* **5** 064401
[60] Chatterjee D, Puphal P, Barthélemy Q, Willwater J, Süllow S, Baines C, Petit S, Ressouche E, Ollivier J, Zoch K M, Krellner C, Parzer M, Riss A, Garmroudi F, Pustogow A, Mendels P, Kermarrec E, and Bert F 2023 *Phys. Rev. B* **107** 125156
[61] Kremer R K, Bette S, Nuss J, and Puphal P 2025 *Phys. Rev. B* **111** 024424

[62] Li Z, Han L, Sun Y, Zhang S, Zeng Z, and Li S 2025 *Chin. Phys. Lett.* **42** 027504

[63] Xu A, Shen Q, Liu B, Zeng Z, Han L, Yan L, Luo J, Yang J, Zhou R, and Li S 2024 *Phys. Rev. B* **110** 085146

[64] Zorko A, Pregelj M, Klanjšek M, Gomilšek M, Jagličić Z, Lord J S, Verezhak J A T, Shang T, Sun W, and Mi J X 2019 *Phys. Rev. B* **99** 214441

[65] Zorko A, Pregelj M, Gomilšek M, Klanjšek M, Zaharko O, Sun W, and Mi J X 2019 *Phys. Rev. B* **100** 144420

[66] Arh T, Gomilšek M, Prelovšek P, Pregelj M, Klanjšek M, Ozarowski A, Clark S J, Lancaster T, Sun W, Mi J X, and Zorko A 2020 *Phys. Rev. Lett.* **125** 027203

[67] Zheng X G, Kawae T, Kashitani Y, Li C S, Tateiwa N, Takeda K, Yamada H, Xu C N, and Ren Y 2005 *Phys. Rev. B* **71** 052409

[68] Elhajal M, Canals B, and Lacroix C 2002 *Phys. Rev. B* **66** 014422

[69] Boldrin D, Fåk B, Canévet E, Ollivier J, Walker H C, Manuel P, Khalyavin D D, and Wills A S 2018 *Phys. Rev. Lett.* **121** 107203

[70] Hering M, Ferrari F, Razpopov A, Mazin I I, Valentí R, Jeschke H O, and Reuther J 2022 *npj Comput. Mater.* **8** 10

[71] Zeng Z, Zhou C, Zhou H, Han L, Chi R, Li K, Kofu M, Nakajima K, Wei Y, Zhang W, Mazzone D G, Meng Z Y, and Li S 2024 *Nat. Phys.* **20** 1097

[72] Zeng Z, Ma X, Wu S, Li H F, Tao Z, Lu X, Chen X h, Mi J X, Song S J, Cao G H, Che G, Li K, Li G, Luo H, Meng Z Y, and Li S 2022 *Phys. Rev. B* **105** L121109

[73] Li S, Cui Y, Zeng Z, Wang Y, Hu Z, Liu J, Li C, Xu X, Chen Y, Liu Z, Li S, and Yu W 2024 *Phys. Rev. B* **109** 104403

[74] Lee C, Lee S, Kim H S, Kittaka S, Kohama Y, Sakakibara T, Lee K H, van Tol J, Gorbunov D I, Do S H, Yoon S, Berlie A, and Choi K Y 2023 *Phys. Rev. B* **107** 214404

[75] Suetsugu S, Asaba T, Ikemori S, Sekino Y, Kasahara Y, Totsuka K, Li B, Zhao Y, Li Y, Kohama Y and Matsuda Y 2024 arXiv:2407.16208 [cond-mat.str-el]

[76] Jeon S, Wulferding D, Choi Y, Lee S, Nam K, Kim K H, Lee M, Jang T H, Park J H, Lee S, Choi S, Lee C, Nojiri H, and Choi K Y 2024 *Nat. Phys.* **20** 435

[77] Han L, Zeng Z, Zhou C, Liu B, Kofu M, Nakajima K, Steffens P, Hiess A, Meng Z Y, Su Y, and Li S 2024 arXiv:2411.09883 [cond-mat.str-el]

[78] Zhu W, Chen X, He Y C, and Witczak-Krempa W 2018 *Sci. Adv.* **4** eaat5535

[79] Nomura Y and Imada M 2021 *Phys. Rev. X* **11** 031034

[80] Da Liao Y, Xu X Y, Meng Z Y, and Qi Y 2022 *Phys. Rev. B* **106** 115149

[81] Picot T, Ziegler M, Orús R, and Poilblanc D 2016 *Phys. Rev. B* **93** 060407

[82] Zheng G, Zhu Y, Chen K W, Kang B, Zhang D, Jenkins K, Chan A, Zeng Z, Xu A, Valenzuela O A, Blawat J, Singleton J, Li S, Lee P A, and Li L 2025 *Proc. Natl. Acad. Sci. U.S.A* **122** e2421390122

[83] Nishimoto S, Shibata N, and Hott C 2013 *Nat. Commun.* **4** 2287

[84] Fang D Z, Xi N, Ran S J, and Su G 2023 *Phys. Rev. B* **107** L220401

[85] He L W, Yu S L, and Li J X 2024 *Phys. Rev. Lett.* **133** 096501

[86] Suetsugu S, Asaba T, Kasahara Y, Kohsaka Y, Totsuka K, Li B, Zhao Y, Li Y, Tokunaga M, and Matsuda Y 2024 *Phys. Rev. Lett.* **132** 226701

[87] Zheng G, Zhang D, Zhu Y, Chen K W, Chan A, Jenkins K, Kang B, Zeng Z, Xu A, Ratkovski D, Blawat J, Bangura A, Singleton J, Lee P A, Li S, and Li L 2024 arXiv:2409.05600 [cond-mat.str-el]

[88] Motrunich O I 2006 *Phys. Rev. B* **73** 155115

[89] Hong X, Behnami M, Yuan L, Li B, Brenig W, Büchner B, Li Y, and Hess C 2022 *Phys. Rev. B* **106** L220406